

1 **Rheologic constraints on the upper mantle from five years of**
2 **postseismic deformation following the El Mayor-Cucapah**
3 **earthquake**

4 **T. T. Hines¹, E. A. Hetland¹**

5 ¹Department of Earth and Environmental Sciences, University of Michigan, Ann Arbor, Michigan, USA.

6 **Key Points:**

- 7 • = enter point 1 here =
8 • = enter point 2 here =
9 • = enter point 3 here =

10 **Abstract**

11 Five years of postseismic deformation following the Mw7.2 El Mayor-Cucapah earthquake re-
 12 veals transient deformation that decays back to its pre-earthquake trend after ~ 3 years at epi-
 13 central distances greater than ~ 200 km. At closer distances, the rapid transience decays to a
 14 sustained rate which exceeds its pre-earthquake trend. We attempt to determine the mecha-
 15 nisms driving this deformation, where we consider afterslip at seismogenic depths and viscoelas-
 16 tic relaxation in the lower crust and upper mantle as candidate mechanisms. We find that early,
 17 rapid, near-field deformation can be explained with afterslip on the fault that ruptured coseis-
 18 mically, while the later, sustained, near-field deformation can be explained with either contin-
 19 ued afterslip in an effectively elastic lower crust, or lower crustal viscoelastic relaxation with
 20 a steady-state viscosity of $\sim 10^{19}$ Pa s. The trend in far-field deformation is best explained with
 21 a transient viscosity of $\sim 10^{18}$ Pa s in the upper mantle. We argue that a transient rheology
 22 in the mantle is preferable over a Maxwell rheology because it better predicts the decay in post-
 23 seismic deformation, and also because it does not conflict with the generally higher, steady-
 24 state viscosities inferred from studies of geophysical processes occurring over longer time-scales.

25 **1 Introduction**

26 Ground deformation in the years following a large (\gtrsim Mw7) earthquake provides insight
 27 into the mechanical behaviour of the crust and upper mantle. It has long been recognized that
 28 interpretations of postseismic deformation can be ambiguous because multiple postseismic de-
 29 formation mechanisms can have qualitatively similar surface expressions [e.g. Savage, 1990].
 30 Owing to the dense geodetic network deployed throughout the 2000s as part of the Plate Bound-
 31 ary Observatory, the postseismic deformation following the April 4, 2010, Mw7.2 El Mayor-
 32 Cucapah earthquake in Baja California was observed at more GPS stations than any other earth-
 33 quake in California to date. With such a large collection of data, we attempt to discern the mech-
 34 anisms driving postseismic deformation following the El Mayor-Cucapah earthquake, where
 35 we consider both afterslip and viscoelastic relaxation in the lower crust and upper mantle as
 36 candidate mechanisms.

37 Previous studies which have modelled postseismic deformation following the El Mayor-
 38 Cucapah earthquake include Pollitz *et al.* [2012], Gonzalez-Ortega *et al.* [2014], Spinler *et al.*
 39 [2015], and Rollins *et al.* [2015]. Of these studies, Gonzalez-Ortega *et al.* [2014] and Rollins
 40 *et al.* [2015] have attempted to describe the postseismic deformation with afterslip in an elas-
 41 tic half-space. Gonzalez-Ortega *et al.* [2014] described five months of postseismic deforma-
 42 tion, observed by InSAR and GPS within ~ 50 km rupture, with afterslip and contraction on
 43 the coseismically ruptured fault. Gonzalez-Ortega *et al.* [2014] noted that their preferred model
 44 underestimated the GPS displacements for stations $\gtrsim 25$ km from the rupture and suggested
 45 that it could be the result of unmodelled viscoelastic relaxation. Using only continuous GPS
 46 stations, which are mostly north of the rupture zone, Rollins *et al.* [2015] found that three years
 47 of postseismic deformation can be adequately explained by afterslip, albeit with an implau-
 48 sibly large amount of slip inferred on the least constrained, southern-most fault segment. Here,
 49 we suggest the afterslip inferred by Rollins *et al.* [2015] may have been acting as a proxy for
 50 distributed relaxation in the upper mantle.

51 Pollitz *et al.* [2012], Rollins *et al.* [2015] and Spinler *et al.* [2015] have explored viscoelas-
 52 tic relaxation in the lower crust and upper mantle as a potential postseismic deformation mech-
 53 anism. The rheology of the crust and mantle is largely unknown and so modelling postseis-
 54 mic deformation with viscoelastic relaxation requires one to assume a rheologic model and
 55 then find the best fitting rheologic parameters. The inference of these rheologic parameters is
 56 a computationally expensive non-linear inverse problem which is typically approached with
 57 a forward modelling grid search method. Consequently, a simplified structure for the lithosphere
 58 must be assumed in order to minimize the number of rheologic parameters that need to be es-
 59 timated. For example, it is commonly assumed that the lithosphere consists of only three ho-
 60 mogeneous, Maxwell viscoelastic layers, which may be an inadequate representation of the

lithosphere [Riva and Govers, 2009; Hines and Hetland, 2013]. To further reduce the dimensions of the model space, it is also necessary to make simplifying assumptions about the nature of afterslip. For example, one can assume a frictional model for afterslip and parametrize afterslip in terms of the unknown rheologic properties of the fault [e.g. Johnson *et al.*, 2009; Johnson and Segall, 2004]. One can also assume that afterslip does not persist for more than a few months and then model the later postseismic deformation assuming it to be the result of only viscoelastic relaxation [e.g. Pollitz *et al.*, 2012; Spinler *et al.*, 2015]. However, postseismic afterslip in similar tectonic settings has been observed to persist for decades following earthquakes [Çakir *et al.*, 2012; Cetin *et al.*, 2014]. Indeed, the preferred viscoelastic model from Pollitz *et al.* [2012] significantly underestimates deformation in the Imperial Valley, which could be indicative of unmodelled continued afterslip. Neglecting to allow for sustained afterslip as a postseismic mechanism could then lead to biased inferences of lithospheric viscosities.

In this study, we assume that both afterslip and viscoelastic relaxation can contribute to postseismic deformation. Modelling both of these mechanisms creates a high dimensional model space that must be searched with non-linear optimization methods. We first develop an initial postseismic model using the method described in Hines and Hetland [2016]. This method simultaneously estimates the afterslip and effective lithospheric viscosity structure necessary to describe early postseismic deformation. Our initial model describes the first 0.8 years of postseismic deformation following the El Mayor-Cucapah earthquake. We then use the inferred effective viscosity structure from the initial model to create a suite of postseismic models to explain the 5 years of postseismic data available to date. Of the suite of models tested, we find that postseismic deformation following the El Mayor-Cucapah earthquake can be explained with afterslip on a fault segment running through the Sierra Cucapah, a Zener rheology in the upper mantle with a transient viscosity that decays from 5×10^{18} Pa s to 1×10^{18} Pa s at 120 km depth, and a relatively stronger lower crust.

2 Data Processing

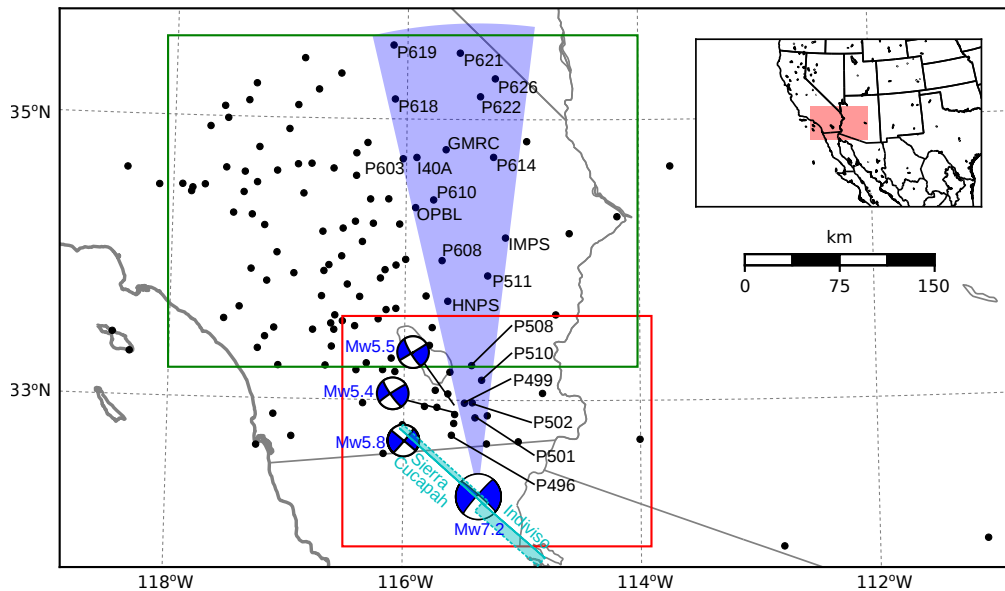
We use continuous GPS position time series provided by University Navstar Consortium (UNAVCO) for stations within a 400 km radius about the El Mayor-Cucapah epicentre. We collectively describe the coseismic and postseismic displacements resulting from the El Mayor-Cucapah earthquake as $u_{\text{post}}(t)$. We consider the GPS position time series, $u_{\text{obs}}(t)$, to be the superposition of $u_{\text{post}}(t)$, secular tectonic deformation, annual and semi-annual oscillations, and coseismic offsets from significant earthquakes over the time span of this study. The June 14, 2010, Mw5.8 Ocotillo earthquake and the Brawley swarm, which included an Mw5.5 and an Mw5.3 event on August 26, 2012, (Figure 1) are the only earthquakes that produced noticeable displacements in any of the time series. We treat the displacements resulting from the Brawley swarm as a single event because the daily solutions provided by UNAVCO cannot resolve the separate events. Although the Ocotillo earthquake had its own series of aftershocks [Hauksson *et al.*, 2011], neither the Ocotillo earthquake nor the Brawley swarm produced detectable postseismic deformation, and we model displacements resulting from these events with only a Heaviside function, $H(t)$, describing the coseismic offsets. We then model $u_{\text{obs}}(t)$ as

$$u_{\text{obs}}(t) = u_{\text{pred}}(t) + \epsilon, \quad (1)$$

where

$$\begin{aligned} u_{\text{pred}}(t) = & u_{\text{post}}(t)H(t - t_{\text{emc}}) + c_0 + c_1 t + \\ & c_2 \sin(2\pi t) + c_3 \cos(2\pi t) + c_4 \sin(4\pi t) + c_5 \cos(4\pi t) + \\ & c_6 H(t - t_{\text{oc}}) + c_7 H(t - t_{\text{bs}}). \end{aligned} \quad (2)$$

In the above equations, t_{emc} , t_{oc} and t_{bs} are the times of the El Mayor-Cucapah earthquake, Ocotillo earthquake, and the Brawley swarm, respectively, c_0 through c_7 are unknown coefficients, and ϵ is the observation noise. We only estimate jumps associated with the Ocotillo earthquake and Brawley swarm for stations within 40 km of their epicentres.



87 **Figure 1.** Map of the region considered in this study. The large focal mechanism is for the El Mayor-
 88 Cucapah earthquake and the three small focal mechanisms are for the Ocotillo earthquake and the two main
 89 shocks during the Brawley swarm. The black dots indicate the locations of GPS stations used in this study.
 90 The fault geometry used in this study is shown in cyan where dashed lines indicate buried edges of the fault
 91 segments. The green and red boxes demarcate the extent of the near-field and far-field maps (figures 4 and 5).
 92 Stations within the blue sector, which highlights the area within 10° of the El Mayor-Cucapah P axis, are used
 93 in the record sections in Figures 7, 10, and 14

99 Stations which recorded displacements that clearly cannot be described by the aforementioned
 100 processes are not included in our analysis. This includes stations in the Los Angeles
 101 basin, where anthropogenic deformation can be larger than the postseismic signal that we are
 102 trying to estimate [Bawden *et al.*, 2001; Argus *et al.*, 2005]. In order to ensure an accurate es-
 103 timation of the secular deformation, we only use stations that were installed at least six months
 104 prior to El Mayor-Cucapah earthquake. Several GPS stations were installed after the El Mayor-
 105 Cucapah earthquake to improve the spatial resolution of postseismic deformation [Spinler *et al.*,
 106 2015]. Although it would be possible to subtract secular velocities derived from elastic block
 107 models [e.g. Meade and Hager, 2005] from velocities recorded at the newly installed stations
 108 to get an estimate of postseismic velocities, we do not do so here. We use coseismic and post-
 109 seismic displacements, rather than velocities, in our inverse method described in Section 3. We
 110 use displacements because estimating velocities from an already noisy displacement time se-
 111 ries can introduce significant uncertainties depending on exactly how the estimation is done.
 112 This choice prevents us from using the newly installed stations in Baja California for our anal-
 113 ysis.

114 The October 16, 1999, Mw7.1 Hector Mine earthquake, which occurred \sim 270 km north
 115 of the El Mayor-Cucapah epicentre, produced transient postseismic deformation which we do
 116 not wish to model, either mechanically or through empirical line fitting. We thus restrict our
 117 analysis to deformation observed six years after the Hector Mine earthquake, which is when
 118 postseismic velocities at sites proximal to the Hector Mine epicentre are approximately con-
 119 stant [Savage and Svare, 2009]. When appraising our model fit in Section 3, we see some sys-
 120 tematic residuals in the vicinity of the Hector Mine epicentre, which may be the result of er-
 121 rors in the assumption that the trend in Hector Mine postseismic deformation is linear after
 122 six years.

Studies of postseismic deformation typically assume a parametric form for $u_{\text{post}}(t)$, such
 as one with a logarithmic or exponential time dependence [e.g. Savage *et al.*, 2005]. However,
 by assuming a logarithmic or exponential form of $u_{\text{post}}(t)$ we run the risk of over fitting the
 GPS time series and inferring a non-existent postseismic signal. We therefore do not assume
 any parametric form for $u_{\text{post}}(t)$ and rather treat it as integrated Brownian motion, so that

$$\dot{u}_{\text{post}}(t) = \sigma^2 \int_0^t w(s) ds, \quad (3)$$

where $w(t)$ is white noise and the variance of $\dot{u}_{\text{post}}(t)$ increases linearly with time by a fac-
 tor of σ^2 . We use a Kalman filtering approach to estimate $u_{\text{post}}(t)$ and the unknown param-
 eters in eq. (2). In the context of Kalman filtering, our time varying state vector is

$$\mathbf{X}(t) = [u_{\text{post}}(t), \dot{u}_{\text{post}}(t), c_0, \dots, c_7] \quad (4)$$

and eq. (2) is the observation function which maps the state vector to the GPS observations.
 We initiate the Kalman filter by assuming a prior estimate of $\mathbf{X}(t)$ at the first time epoch, de-
 noted $\mathbf{X}_{1|0}$, which has a sufficiently large covariance, denoted $\Sigma_{1|0}$, to effectively make our
 prior uninformed. For each time epoch, t_i , Bayesian linear regression is used to incorporate
 GPS derived estimates of displacement with our prior estimate of the state, $\mathbf{X}_{i|i-1}$, to form
 a posterior estimate of the state, $\mathbf{X}_{i|i}$, which has covariance $\Sigma_{i|i}$.

We then use the posterior estimate of the state at time t_i to form a prior estimate of the
 state at time t_{i+1} through the transition function

$$\mathbf{X}_{i+1|i} = \mathbf{F}_{i+1} \mathbf{X}_{i|i} + \delta_{i+1} \quad (5)$$

where

$$\mathbf{F}_{i+1} = \begin{bmatrix} 1 & (t_{i+1} - t_i) & \mathbf{0} \\ 0 & 1 & \mathbf{0} \\ \mathbf{0} & \mathbf{0} & \mathbf{I} \end{bmatrix} \quad (6)$$

and δ_{i+1} is the process noise, which has zero mean and covariance described by

$$\mathbf{Q}_{i+1} = \sigma^2 \begin{bmatrix} \frac{(t_{i+1}-t_i)^3}{3} & \frac{(t_{i+1}-t_i)^2}{2} & \mathbf{0} \\ \frac{(t_{i+1}-t_i)^2}{2} & (t_{i+1}-t_i) & \mathbf{0} \\ \mathbf{0} & \mathbf{0} & \mathbf{0} \end{bmatrix}. \quad (7)$$

The covariance of the new prior state, $\mathbf{X}_{i+1|i}$, is then described by

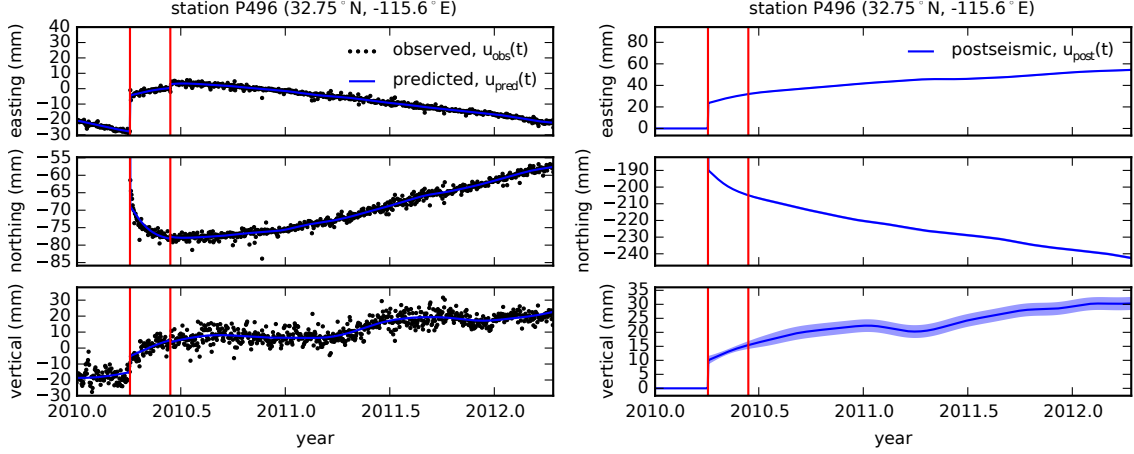
$$\Sigma_{i+1|i} = \mathbf{F}_{i+1} \Sigma_{i|i} \mathbf{F}_{i+1}^T + \mathbf{Q}_{i+1}. \quad (8)$$

This process is repeated for each of the N time epochs at which point we use Rauch-Tung-Striebel smoothing [Rauch *et al.*, 1965] to find $\mathbf{X}_{i|N}$, which is an estimate of the state at time t_i that incorporates GPS observation for all N time epochs. Our final estimates of $u_{\text{post}}(t)$ are used in subsequent analysis, while the remaining components of the state vector are considered nuisance parameters. In the interests of computational tractability, we down sample our smoothed time series from daily solutions down to weekly solutions.

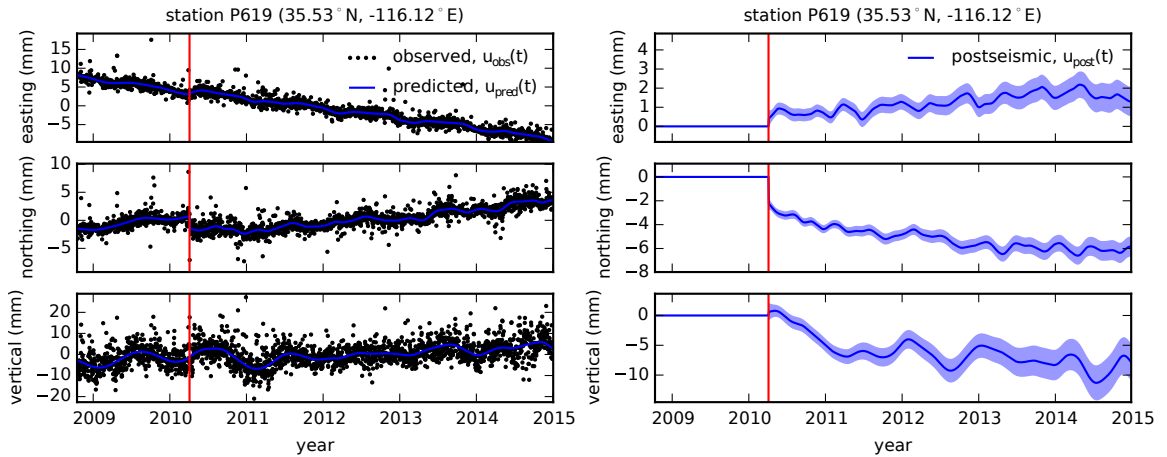
The smoothness of $u_{\text{post}}(t)$ is controlled by the chosen value of σ^2 , which describes how rapidly we expect postseismic displacements to vary over time. Setting σ^2 equal to zero will effectively result in modelling $u_{\text{post}}(t)$ as a straight line which is insufficient to describe the expected transient behaviour in postseismic deformation. The other end member, where σ^2 is infinitely large, will result in $u_{\text{pred}}(t)$ over fitting the data. While one can use a maximum likelihood based approach for picking σ^2 [e.g. Segall and Mathews, 1997], we instead take a subjective approach and choose a value for σ^2 that is just large enough to faithfully describe the observed deformation at the most near-field station in our study, P496, which exhibits the most pronounced rapid changes in velocity. This ensures that σ^2 will be sufficiently large so that our estimate of $u_{\text{post}}(t)$ does not smooth out potentially valuable postseismic signal at the remaining stations. We find that using $\sigma^2 = 0.05 \text{m}^2/\text{yr}^3$ adequately describe all but the first week of postseismic deformation at station P496, which gets incorporated into our estimate of coseismic displacements (Figure 2). By down sampling, we implicitly assume that the first week of deformation is overwhelmingly the result of afterslip and this afterslip is lumped into our estimates of coseismic slip. Freed *et al.* [2007] noted that postseismic deformation can be observed at distances greater than 200 km from the Hector Mine earthquake and, after filtering the time series for stations up to 400 km from the El Mayor-Cucapah epicentre, we also clearly see far reaching postseismic transient deformation (Figure 3).

It is important to note that the shown uncertainties in $u_{\text{post}}(t)$ do not account for the non-negligible epistemic uncertainty in eq. (2). For example, we assume a constant rate of secular deformation, which appears to be an appropriate approximation for all but perhaps the stations closest to the Hector Mine epicentre, as noted above. Also, our model for seasonal deformation in eq. (2) assumes a constant amplitude over time, which means that any yearly variability in the climatic conditions could introduce systematic residuals [Davis *et al.*, 2012]. Indeed, it would be more appropriate to consider the seasonal amplitudes $c_2 - c_5$ in eq. (2) as stochastic variables [Murray and Segall, 2005]. By using constant seasonal amplitudes, our estimate of $u_{\text{post}}(t)$ seems to describe some of the unmodelled annual and semi-annual oscillations (e.g. Figure 3).

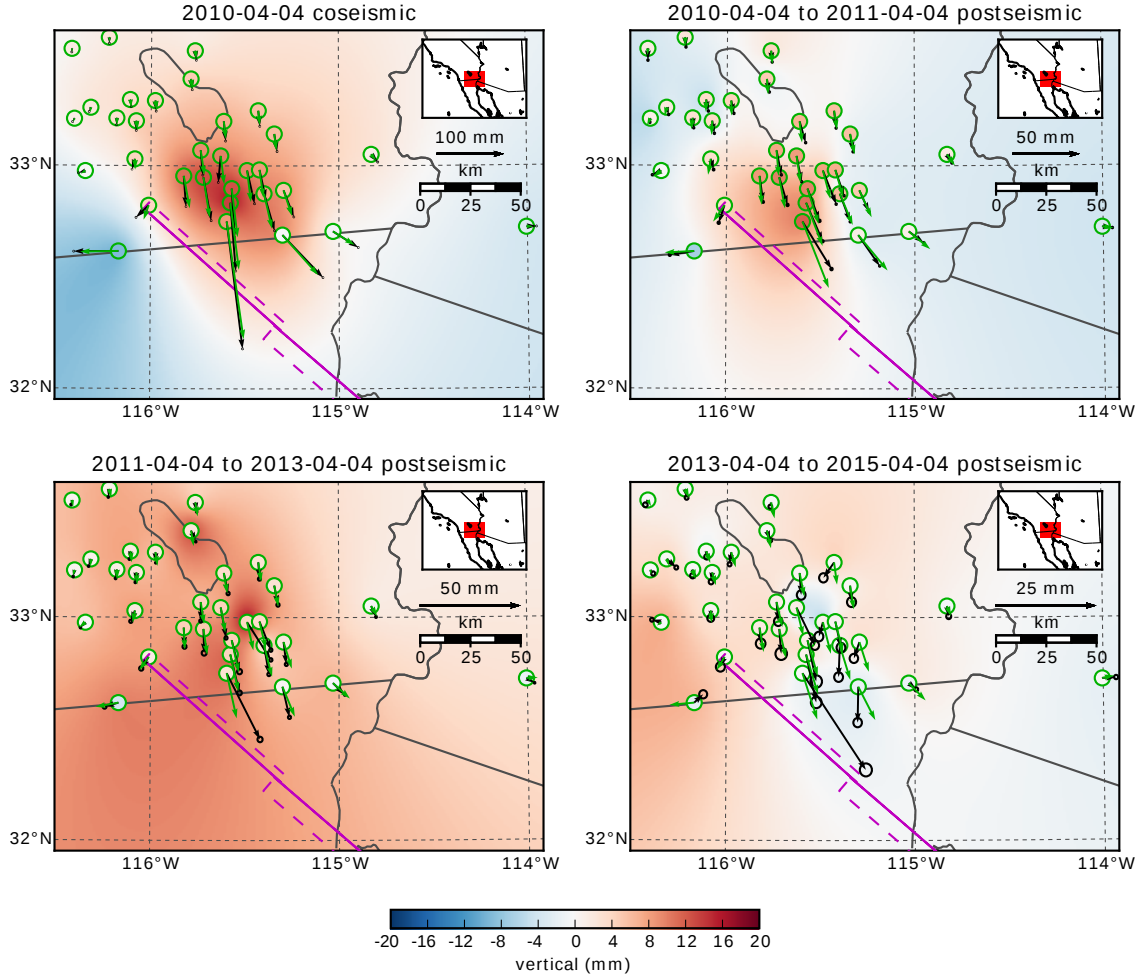
We show in Figures 4 and 5 the near and far-field postseismic displacements accumulated over the time intervals 0-1 years, 1-3 years, and 3-5 years, as well as the coseismic displacements. Stations at epicentral distances ranging from ~ 200 km to as far as ~ 400 km have an elevated rate of deformation for the first 3 years following the earthquake. This far-field deformation has a southward trend along the direction of the El Mayor-Cucapah P axis and a similar eastward trend can be seen in the few far-field stations in Arizona, located along the T axis. After 3 years, the trend in far-field postseismic deformation is barely perceptible. The vertical deformation in the far-field is difficult to attribute to postseismic processes. Most far-field stations display an initial subsidence for the first year after the El Mayor-Cucapah earthquake followed by continued uplift. This trend in vertical deformation can be observed in all



153 **Figure 2.** Left panels show GPS time series from UNAVCO (black) and the predicted displacement (blue)
 154 from eq. (2) for a near-field station. Red lines indicate the times of the El Mayor-Cucapah and Ocotillo earth-
 155 quakes. The right panels show estimated coseismic and postseismic displacements, u_{post} , which are extracted
 156 from the predicted displacements. The 68% confidence interval is shown in light blue.



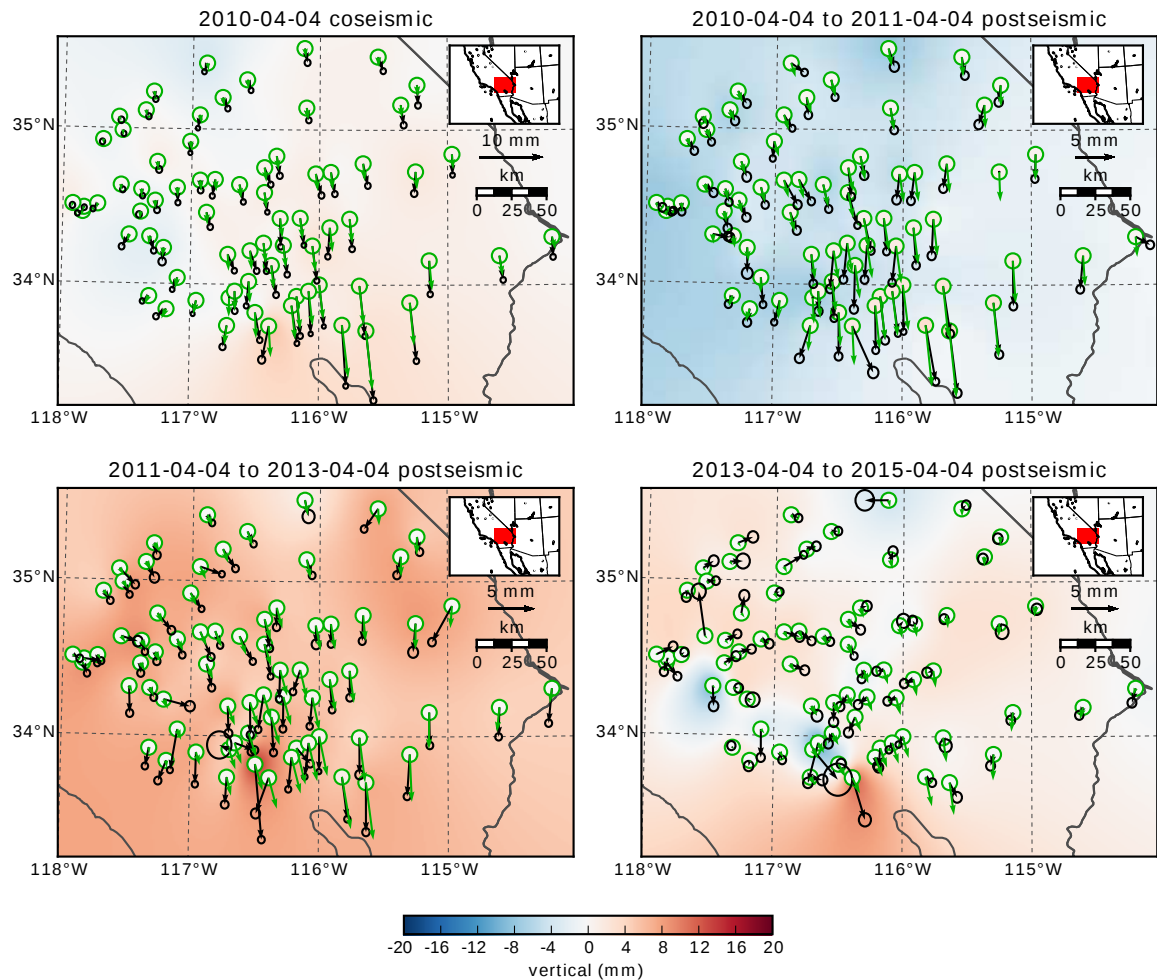
157 **Figure 3.** same as Figure 2 but for a far-field station.



183 **Figure 4.** Near-field coseismic and cumulative postseismic displacements over the indicated time periods
 184 (black) as well as predicted displacements for our preferred model from Section 3.3 (green). Observed verti-
 185 cal deformation is shown as an interpolated field and predicted vertical displacements are shown within the
 186 circles at the base of each vector. Note that the interpolant is not well constrained in Mexico where there is no
 187 data available.

178 three of the quadrants where postseismic data is available, which means that the vertical de-
 179 formation does not exhibit an anti-symmetric quadrant pattern, as would be expected for post-
 180 seismic processes. Although we use vertical deformation in our analysis in Section 3, we do
 181 not put an emphasis on trying to describe the vertical deformation as it likely does not have
 182 postseismic origins.

189 The near-field postseismic deformation is notably sustained when compared to the far-
 190 field deformation. Namely, the station in this study which is closest to the El Mayor-Cucapah
 191 epicentre, P496, has been moving at a steady rate of ~ 1.5 cm/yr to the south since ~ 1 year
 192 after the El Mayor-Cucapah earthquake. Vertical postseismic deformation in the near-field does
 193 display a quadrant pattern which is consistent with the coseismic vertical deformation, sug-
 194 gesting that it is resulting from tectonic processes. However, the vertical postseismic signal
 195 is only apparent for the first year after the earthquake (Figure 4). As with the far-field defor-
 196 mation, there is a general trend of uplift in the near-field after ~ 1 year, which we do not con-
 197 sider to be related to postseismic processes.

**Figure 5.** Same as Figure 4 but for far-field stations.

depth (km)	λ (GPa)	μ (GPa)	η_{eff} (10^{18} Pa s)	μ_k/μ
0-5	24.0	24.0	-	-
5-15	35.0	35.0	-	-
15-30	42.0	42.0	44.3	0.0
30-60	61.0	61.0	5.91	0.375
60-90	61.0	61.0	1.99	0.375
90-120	61.0	61.0	1.31	0.375
120-150	61.0	61.0	1.10	0.375
150- ∞	61.0	61.0	1.07	0.375

Table 1. Assumed and estimated material properties. λ and μ are assumed known *a priori* and are based on the values used for the coseismic model by *Wei et al.* [2011b]. The values for η_{eff} are estimated in Section 3.2 and $\frac{\mu_k}{\mu}$ are the optimal shear moduli ratios found in Section 3.3 for a Zener rheology upper mantle.

3 Postseismic Modeling

In this paper, we seek to find the mechanisms driving 5 years of postseismic deformation following the El Mayor-Cucapah earthquake. We consider afterslip and viscoelastic relaxation in the lithosphere and asthenosphere as candidate mechanisms. Poroelastic rebound has also been used to model postseismic deformation [e.g. Jónsson *et al.*, 2003]; however, *Gonzalez-Ortega et al.* [2014] found that poroelastic rebound is unlikely to be a significant contributor to postseismic deformation following the El Mayor-Cucapah earthquake. Furthermore, we consider stations which are sufficiently far away from the main rupture that poroelastic rebound should be insignificant.

We estimate coseismic and time-dependent postseismic fault slip, both of which are assumed to occur on a fault geometry modified from *Wei et al.* [2011b]. Field studies [*Fletcher et al.*, 2014] and LIDAR observations [*Oskin et al.*, 2012] have revealed a significantly more complicated fault geometry than what was inferred by *Wei et al.* [2011b], especially within the Sierra Cucapah. However, we find that a relatively simple coseismic fault geometry based on [*Wei et al.*, 2011b] is adequate because most of the stations used in this study are sufficiently far from the El Mayor-Cucapah rupture zone that they are insensitive to the details in the fault geometry found by *Fletcher et al.* [2014] and *Oskin et al.* [2012]. The fault geometry used in this study (Figure 1) consists of the two main fault segments inferred by *Wei et al.* [2011b], where the northern segment runs through the Sierra Cucapah up to the US-Mexico border and the southern segment is the Indiviso fault which extends down to the Gulf of California. Both segments extend from the surface to 15 km depth. We extend the northern segment by 40 km to the north-west, motivated by the clustering of aftershocks on the northern tip of the coseismic rupture zone [*Hauksson et al.*, 2011; *Kroll et al.*, 2013]. This extended fault segment was also found to be necessary by *Rollins et al.* [2015] and *Pollitz et al.* [2012] in order to describe the postseismic deformation.

3.1 elastic inversion

We consider a variety of rheologic models for the lower crust and upper mantle. The simplest rheologic model is to consider them to be effectively elastic and isotropic. In such case, the rheologic parameters consist of the Lamé parameters, λ and μ , which are reasonably well known and we use the same values used by *Wei et al.* [2011b], which are listed in Table 3, throughout this paper. The only unknown is the distribution of fault slip, which can be easily estimated from postseismic deformation through linear least squares. Using a subset of the GPS stations considered in this study, *Rollins et al.* [2015] found that 3 years of postseismic deformation following the El Mayor-Cucapah earthquake can be explained with afterslip on the coseismic fault plane without requiring any viscoelastic relaxation. We also perform

an elastic slip inversion, but we use GPS stations within a larger radius about the El Mayor-Cucapah epicentre (400 km instead of ~ 200 km). Our forward problem describing predicted postseismic deformation, u_{pred} , in terms of time dependent fault slip, s , is

$$u_{\text{pred}}(x, t) = \int_F s(\xi, t)g(x, \xi)d\xi \quad (9)$$

where $g(x, \xi)$ is elastic Green's function describing displacement at surface position x resulting from a unit of slip at ξ on the fault, which is denoted by F . We estimate coseismic slip and the rate of afterslip at the discrete time intervals, 0.0-0.125, 0.125-0.25, 0.5-1.0, 1.0-2.0, 2.0-3.0, 3.0-4.0, and 4.0-5.0 years after the earthquake. Each fault segment is discretized into roughly 4 km by 4 km patches and we estimate a strike-slip and thrust component of slip for each patch. We impose that the direction of slip and slip rate are within 45° of right-lateral. We also add zeroth order Tikhonov regularization so that our solution for s satisfies

$$\min_s \left(\left\| \frac{u_{\text{pred}}(s) - u_{\text{post}}}{\sigma_{\text{obs}}} \right\|_2^2 + \lambda_s \|s\|_2^2 \right). \quad (10)$$

The penalty parameters, λ_s , is chosen with a trade-off curve. We use Pylith [Aagaard *et al.*, 2013] to compute the Green's functions for this inversion, as well as for the remaining inversions in this paper.

Our coseismic slip and afterslip solutions are shown in Figure 6. As with Rollins *et al.* [2015], we find that a large amount of afterslip on the southern fault segment is required to explain the observations. The potency of our inferred coseismic slip is $3.2 \times 10^9 \text{ m}^3$, equivalent to a Mw7.28 earthquake when assuming a shear modulus of 32 GPa. The potency of our inferred cumulative 5 years of afterslip is $6.1 \times 10^9 \text{ m}^3$, equivalent to a Mw7.46 earthquake, which is unrealistically large if we consider afterslip to be driven by coseismically induced stresses. Figure 7 shows the time series for the observed and predicted postseismic displacements at stations along the El Mayor-Cucapah P axis. We show the radial component of displacements with respect to the El Mayor-Cucapah epicentre and we also rescale the displacements so that the difference between the minimum and maximum observed displacements are the same for each station. Our elastic slip model accurately describes near-field postseismic deformation, while it systematically underestimates postseismic deformation for stations further than ~ 150 km from the El Mayor-Cucapah epicentre. When the fault segments used in the inversion are extended down to 30 km depth, rather than 15 km, the systematic far-field residuals are smaller but remain apparent. Because an elastic model for the lithosphere requires an unrealistic amount of afterslip and is unable to predict far-field deformation, we move on to consider viscoelastic models in the next section.

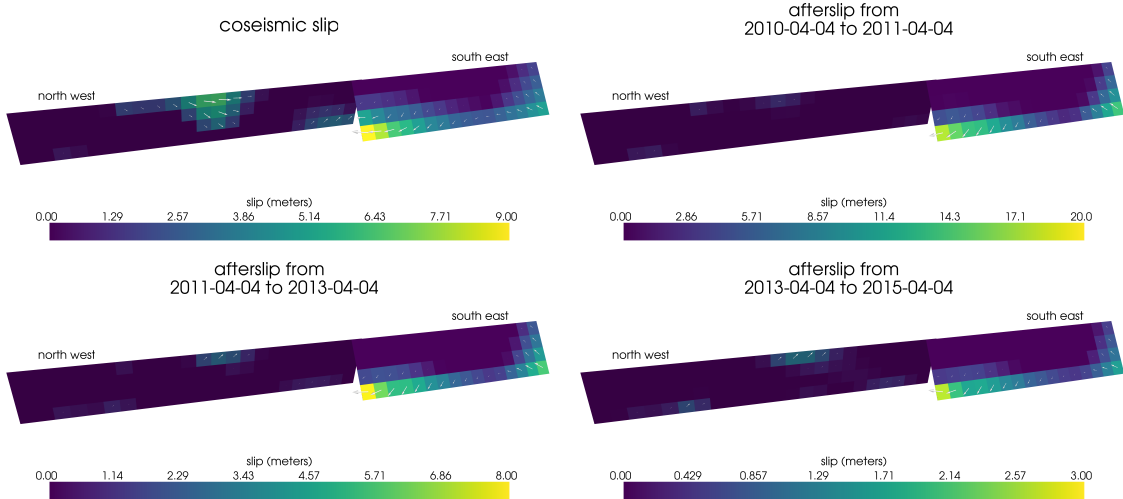
3.2 constraints on effective viscosity

For any linear viscoelastic rheology of the crust and mantle, postseismic displacements resulting from time dependent fault slip can be described as

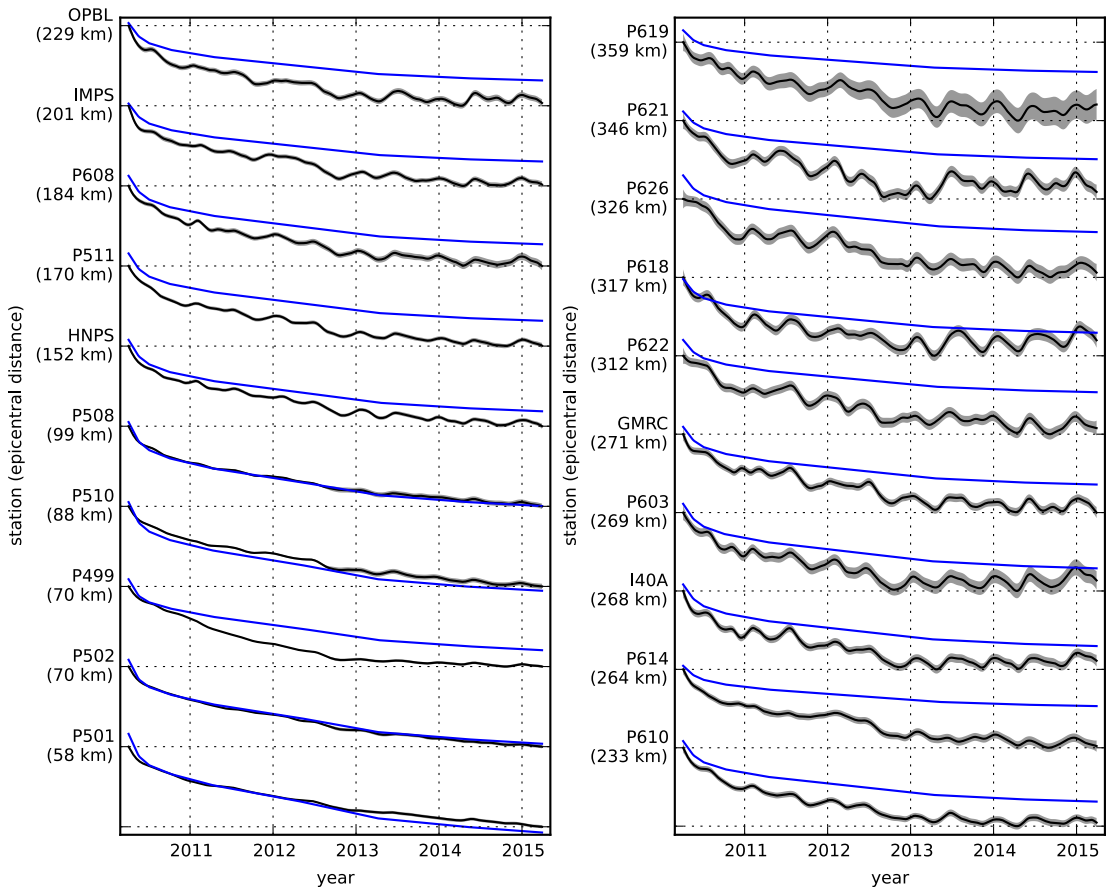
$$u_{\text{pred}}(x, t) = \int_F s(\xi, t)g(x, \xi)d\xi + \int_0^t \int_F s(\xi, \tau)f(t - \tau, x, \xi)d\xi d\tau \quad (11)$$

where $f(t, x, \xi)$ describes the time-dependent velocity at x resulting from viscoelastic relaxation of stresses induced by slip at ξ . f is a function of λ , μ , and any additional rheologic parameters controlling the viscoelastic response, which are generally not well known. Schematic representations of the viscoelastic rheologic models considered in this study are shown in Figure 8. We consider Maxwell viscoelasticity, where the steady-state viscosity, η_M , is unknown, Zener viscoelasticity, where the transient viscosity, η_K , and transient shear modulus, μ_K , are unknown, and Burgers viscoelasticity, where η_M , η_K , and μ_K , are all unknown. We further discuss these rheologic models and their use in geophysical studies in Section 4.

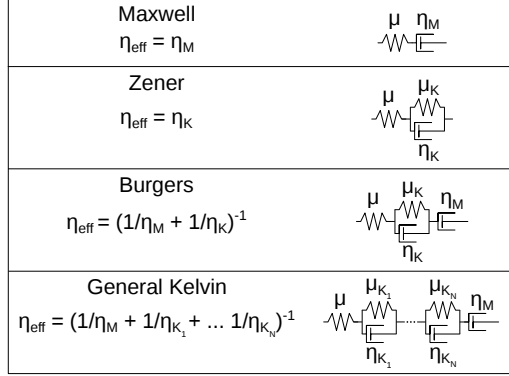
In order to greatly simplify the inverse problem, we use the method described in Hines and Hetland [2016] to constrain an initial effective lithospheric viscosity structure from the



247 **Figure 6.** Coseismic slip and cumulative afterslip over the indicated intervals for the elastic model from
248 Section 3.1. Color indicates the magnitude of slip while arrows indicate the motion of the hanging wall.



249 **Figure 7.** Scaled record section for the radial component of observed postseismic displacements, u_{obs}
250 (black) and displacements predicted by an elastic model, u_{pred} (blue). Downward motion indicates that the
251 station is moving toward the El Mayor-Cucapah epicentre. Displacement time series are scaled so that the
252 minimum and maximum observed values lie on the grid lines. The standard deviation of observed displace-
253 ments are shown in gray.



263 **Figure 8.** Schematic illustration of rheologic models considered in this paper as well as their initial effec-
 264 tion viscosities, $\eta_{\text{eff}} = \frac{\sigma}{\dot{\epsilon}}|_{t=0}$.

early postseismic deformation. Our method utilizes the fact that coseismic stresses throughout the crust and upper mantle depend on the instantaneous elastic parameters and are independent of the viscoelastic parameters which we wish to estimate. Immediately following an earthquake, each parcel will have a strain rate that is proportional to the coseismic stress and inversely proportional to the parcel's effective viscosity, η_{eff} . Using one-dimensional viscoelastic models, we define the effective viscosity as

$$\eta_{\text{eff}} = \left. \frac{\sigma}{\dot{\epsilon}} \right|_{t=0} \quad (12)$$

where σ is an applied stress at $t = 0$ and $\dot{\epsilon}$ is the resulting strain rate. Figure 8 shows how η_{eff} relates to the parameters for various linear viscoelastic rheologies. We can deduce that the initial rate of surface deformation resulting from viscoelastic relaxation is a summation of the surface deformation resulting from relaxation in each parcel, scaled by the reciprocal of the parcel's effective viscosity. That is to say

$$f(0, x, \xi) = \int_L \frac{h(x, \xi, \zeta)}{\eta_{\text{eff}}(\zeta)} d\zeta, \quad (13)$$

where L denotes the crust and mantle and $h(x, \xi, \zeta)$ describes the initial rate of deformation resulting from viscoelastic relaxation at ζ induced by slip at ξ . We can combine eq. (13) with eq. (11) to get a first order approximation for early postseismic deformation,

$$u_{\text{pred}}(x, t) \approx \int_F s(\xi, t) g(x, \xi) d\xi + \int_0^t \int_F \int_L \frac{s(\tau, \xi)}{\eta_{\text{eff}}(\zeta)} h(x, \xi, \zeta) d\zeta d\xi d\tau, \quad (14)$$

265 which is valid for as long as the rate of deformation resulting from viscoelastic relaxation is
 266 approximately constant.

267 Details on how eq. (14) is used to estimate s and η_{eff} from postseismic deformation can
 268 be found in *Hines and Hetland* [2016]. A non-linear Kalman filter based inverse method can
 269 also be used to estimate s and η_{eff} in a manner akin to *Segall and Mathews* [1997] or *McGuire*
 270 and *Segall* [2003], in which we would not have to explicitly impose a time dependent parametriza-
 271 tion of s . We have thoroughly explored Kalman filter based approaches, but we ultimately pre-
 272 fer the method described in *Hines and Hetland* [2016] because of its relative simplicity. More-
 273 over, we believe the piecewise continuous representation of slip with respect to time to be suf-
 274 ficiently general for the resolving power of these GPS data.

275 Although eq. (14) may only be valid for a short portion of the postseismic period, its
 276 utility becomes apparent when noting that g and h are only functions of the fault geometry
 277 and instantaneous elastic properties, λ and μ , and thus g and h can be computed numerically

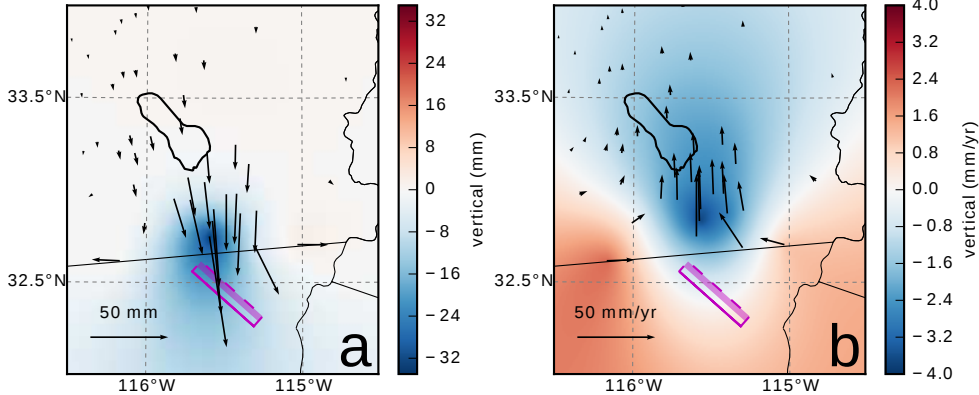
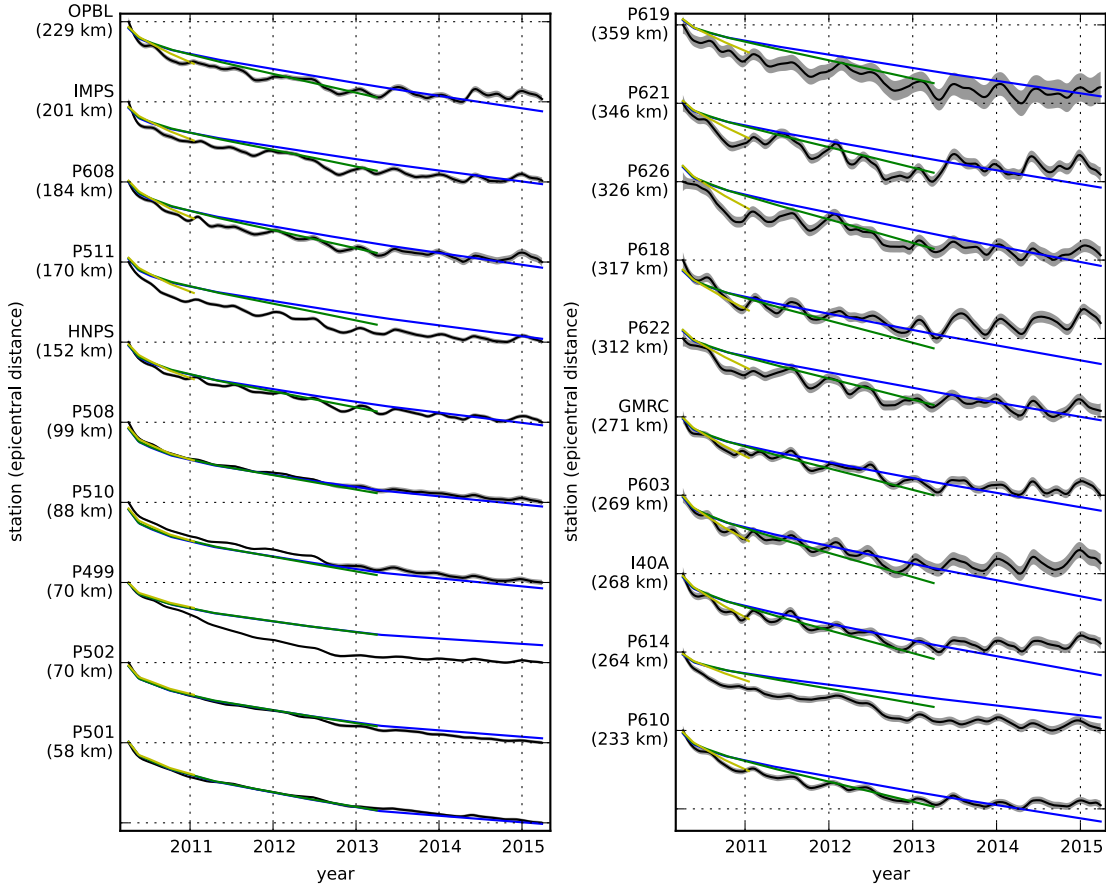


Figure 9. Displacements resulting from fault slip at lower crustal depths (left), and initial velocities resulting from subsequent relaxation of a viscoelastic lower crust (right). The fault segment dips 75° to the north east and its surface projection is outlined in green. The highlighted area on the fault extends from 15 to 30 km depth and indicates where 1 meter of right-lateral slip was imposed. The elastic properties of the crust and mantle are the same as in Table 3 and $\eta_{\text{eff}} = 10^{18}$ Pa s in the lower crust. Vertical displacements are interpolated between station locations.

as a preprocessing step. The forward problem in eq. (14) can be rapidly evaluated for any realization of s and η_{eff} . This is in contrast to evaluating the full forward problem, eq. (11), numerically for each realization of s and unknown rheologic properties.

We perform an initial inversion of postseismic displacements using the approximation in eq. (14). We estimate coseismic slip and afterslip with the same spatial and temporal discretization as in Section 3.1. Simultaneously, we estimate η_{eff} within six vertically stratified layers which have depths ranging from 15-30 km, 30-60 km, 60-90 km, 90-120 km, 120-150 km, as well as from 150 km to the bottom of our numerical model domain at 800 km. We again restrict fault slip to occur between 0 and 15 km depth, which is done in order to help eliminate inevitable non-uniqueness in the inversion. It has long been recognized that fault slip at sufficiently great depths can produce surface deformation that is indistinguishable from viscoelastic relaxation, at least in two-dimensional earthquake models [Savage, 1990]. Additionally, we note that when simultaneously estimating both afterslip and viscosity in the lower crust, the inverse problem becomes particularly ill-posed. This ill-posedness is illustrated in Figure (9), which shows the displacements resulting from a meter of slip on a fault extending from 15 to 30 km depth and the initial velocity resulting from subsequent viscoelastic relaxation in the lower crust, which is given a viscosity of 10^{18} Pa s. In this demonstration, the viscoelastic relaxation is entirely driven by the fault slip in the lower crust. The horizontal displacements from fault slip are in the opposite direction as the displacements resulting from viscoelastic relaxation. This means that surface displacements resulting from afterslip at lower crustal depths can be cancelled out, at least partially, by a low viscosity lower crust. We eliminate this null space by allowing only one mechanism in the lower crust, which we choose to be viscoelastic relaxation. This is not to say that we do not believe deep afterslip to be a possibility, rather we restrict slip to seismogenic depths as a modelling necessity. Although, it has been noted that the pattern of vertical postseismic deformation following the El Mayor-Cucapah earthquake indicates that a significant amount of afterslip must be shallow [Rollins et al., 2015].

The first step in our inverse method is to determine at which point the early postseismic approximation breaks down, which we will denote as t_{bd} . As noted, it is valid for approximately as long as the rate of deformation resulting from viscoelastic relaxation is approximately constant. We can almost certainly assume that deformation at the most far-field stations, which are ~ 400 km away from the El Mayor-Cucapah epicentre, is the result of vis-



333 **Figure 10.** Observed postseismic displacements (black) and best fitting predictions of eq. (14) to 5.0 (blue),
 334 3.0 (green), and 0.8 (yellow) years of the postseismic data.

315 coelastic relaxation. The approximation should then be valid for as long as a linear trend ad-
 316 equately approximates the far-field deformation. Using this logic, it would appear that $t_{bd} \approx$
 317 1 year after the El Mayor-Cucapah earthquake. Another way to determine t_{bd} is to find the
 318 best fitting prediction of eq. (14) to observed deformation using increasing durations of the
 319 postseismic time series. t_{bd} should be the point when eq. (14) is no longer capable of describ-
 320 ing the observed deformation without incurring systematic misfits. When using eq. (14) to fit
 321 the entire 5 years of postseismic displacements, we see that the near-field displacements (e.g.,
 322 station P501) are accurately predicted but when looking at displacement in the far-field (e.g.,
 323 station P621) we see that eq. (14) overestimates the rate of deformation in the later postseis-
 324 mic period and underestimates the rate of deformation in the early period (Figure 10). Due
 325 to the low signal-to-noise ratios for far-field stations, it is difficult to determine at what point
 326 eq. (14) is no longer able to predict the observed displacements without incurring any signif-
 327 icant systematic misfit; however, we settle on $t_{bd} = 0.8$ years after the earthquake, while ac-
 328 knowledging that the choice is subjective. As noted in *Hines and Hetland* [2016], overestimat-
 329 ing t_{bd} will result in a bias towards overestimating η_{eff} , while picking a t_{bd} which is too low
 330 will not necessarily result in a biased estimate of η_{eff} , although the uncertainties would be larger.
 331 We can then consider inferences of η_{eff} to be an upper bound on the viscosity needed to de-
 332 scribe the far-field rate of deformation during the first 0.8 years of postseismic deformation.

We estimate coseismic slip, afterslip, and effective viscosity by solving

$$\min_{s, \eta_{\text{eff}}} \left(\left\| \frac{u_{\text{pred}}(s, \eta_{\text{eff}}) - u_{\text{obs}}}{\sigma_{\text{obs}}} \right\|_2^2 + \lambda_s \|s\|_2^2 + \lambda_\eta \|\nabla \eta_{\text{eff}}^{-1}\|_2^2 \right) \quad (15)$$

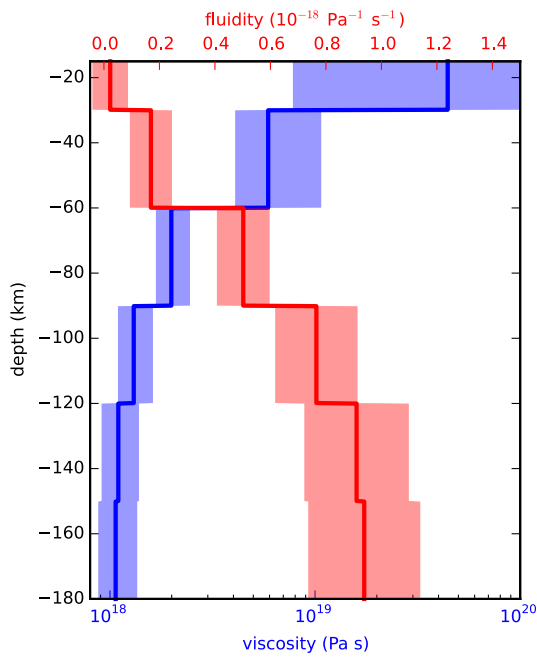
where u_{obs} consists of the first 0.8 years of postseismic deformation and u_{pred} are the predicted displacements from eq. (14). Due to inherent non uniqueness, we have added zeroth-order Tikhonov regularization to estimates of s , and second-order Tikhonov regularization to estimates of effective fluidity, η_{eff}^{-1} . The degree to which we impose the regularization on slip and fluidity is controlled by the penalty parameters λ_s and λ_η . The penalty parameters are chosen with two trade-off curves. We first choose λ_s while fixing λ_η at 0 and then we determine λ_η with λ_s fixed at its chosen value. Our goal here is to get a prior constraint on η_{eff} to minimize the amount of searching we have to do when describing the postseismic deformation over the full 5 years, which we do in Section 3.3. Estimates of s made here will not be used in Section 3.3, and so the motivation behind adding regularization to s is to ensure that the slip driving viscoelastic relaxation in eq. (14) is sensible.

Our inferred estimates of effective viscosities, and corresponding fluidities, are shown in Figure 11. Although fluidity is rarely used in geophysical literature, eq. (13) is linear with respect to fluidity and so the fluidity indicates the amplitude of the viscoelastic signal coming from each layer. We also show 95% confidence intervals for estimated viscosities and fluidities but we note that the uncertainties tend to be underestimated due to the added regularization [Aster *et al.*, 2011]. Although, we do believe that the relative uncertainty between layers is accurately depicted. A robust feature that we see is that the largest jump in fluidity is at 60 km depth, which is consistent with the range of lithosphere-asthenosphere boundary depths inferred by Lekic *et al.* [2011]. This transitional depth is also consistent with the the viscosity structure required to explain far field postseismic deformation following the Hector Mine earthquake [Freed *et al.*, 2007]. We find that the viscosity below 60 km depth needs to be $\sim 1 \times 10^{18}$ Pa s to describe the early rate of postseismic deformation at far-field stations while the lower crust and uppermost mantle need to be relatively stronger. The viscosity of the lower crust is the least well constrained as there is no evidence of relaxation in that layer, meaning that it is effectively elastic over the first 0.8 years after the earthquake.

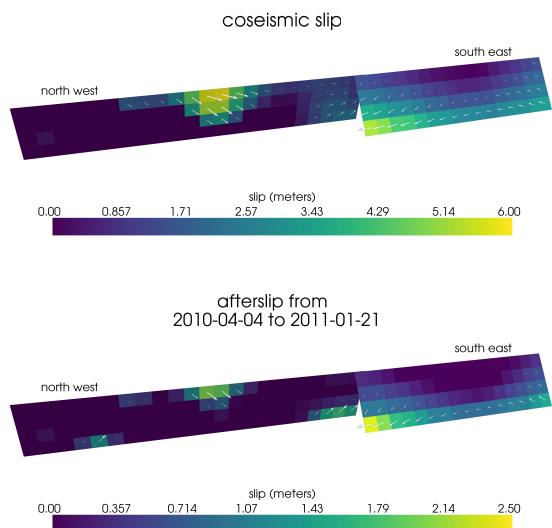
Our initial estimate for coseismic slip and cumulative afterslip over the first 0.8 years after the El Mayor-Cucapah earthquake are shown in Figure 12. Similar to our elastic slip model from Section 3.1, coseismic slip is inferred to be in the Sierra Cucapah and it is right lateral with a significant normal component. This is consistent with field studies [Fletcher *et al.*, 2014], as well as the coseismic slip from Wei *et al.* [2011b]. The potency of inferred coseismic slip is 3.3×10^9 m³, which is also about the same as that inferred from Section 3.1. The present inference of afterslip on the Indiviso fault is significantly less than what was found in the Section 3.1 where we did not account for viscoelasticity. When fault slip is simultaneously estimated with a lithospheric and asthenospheric viscosity, the potency of inferred afterslip over the first 0.8 years after the earthquake is 0.85×10^9 m³, compared to 3.46×10^9 m³ when we assume the lithosphere and asthenosphere are elastic. The significant amount of afterslip inferred on the Indiviso fault seems to be compensating for unmodelled viscoelastic relaxation at depths greater than 60 km. The fact that there is still an appreciable amount of afterslip inferred on the Indiviso fault even when allowing for viscoelastic relaxation in the lower crust and upper mantle raises the question of whether it is compensating for viscoelastic relaxation that is more localized than what we allow for since we only estimate depth dependent variations in viscosity.

3.3 Full Inversion

In the previous section, we used the inverse method from Hines and Hetland [2016] to constrain the effective viscosity structure required to explain the first 0.8 years of postseismic deformation. In this section, we use these effective viscosities as a prior constraint when searching for models which are capable of describing the available 5 years of postseismic data, where



361 **Figure 11.** Effective viscosities and associated fluidities inferred by fitting eq. (14) to the first 0.8 years of
 362 postseismic displacements. 95% confidence intervals, estimated from bootstrapping, are indicated by color
 363 fields.



381 **Figure 12.** Coseismic slip and afterslip inferred by fitting eq. (14) to the first 0.8 years of postseismic
 382 displacements.

our forward problem is now eq. (11) rather than the approximation given by eq. (14). We perform a series of coseismic slip and afterslip inversion assuming a variety of rheologies for the lower crust and upper mantle which are consistent with our findings from Section 3.2. We appraise each model using the mean chi-squared value,

$$\bar{\chi}^2 = \frac{1}{N} \left\| \frac{u_{\text{pred}} - u_{\text{obs}}}{\sigma_{\text{obs}}} \right\|_2^2, \quad (16)$$

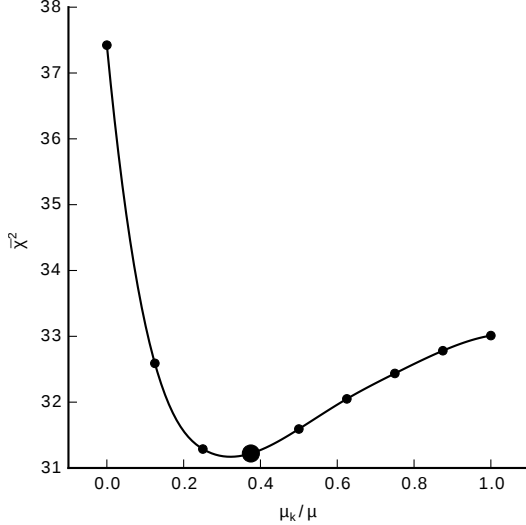
where N is the number of observations.

We first assume that the crust and mantle can be described with a Maxwell rheology, and we set η_M equal to our inference of η_{eff} . We compute f and g from eq. (11) using the finite element software, Pylith [?], and assume the same spatial and temporal discretization of s as in Sections 3.1 and 3.2. We estimate s using linear least squares and we find $\bar{\chi}^2 = 37.4$. For comparison, $\bar{\chi}^2 = 35.3$ for the elastic model from Section 3.1. The Maxwell viscoelastic model has a larger misfit because it tends to overestimate the rate of deformation after about 3 years (Figure 14). Since our initial estimates of η_{eff} may be biased towards overestimating viscosities, we have also performed the slip inversion where we use uniformly lower viscosities in the crust and mantle. However, decreasing the viscosity only increases the misfit. Although, the viscosities used here are consistent with the successful Maxwell viscoelastic models found by *Rollins et al.* [2015] and *Spinler et al.* [2015], which had mantle viscosities on the order of 10^{18} Pa s, we find that such a model is incapable of describing the entire postseismic time series. *Pollitz et al.* [2001] similarly recognized this deficiency in a Maxwell rheology, which then motivated their exploration of a Burgers rheology upper mantle [*Pollitz*, 2003].

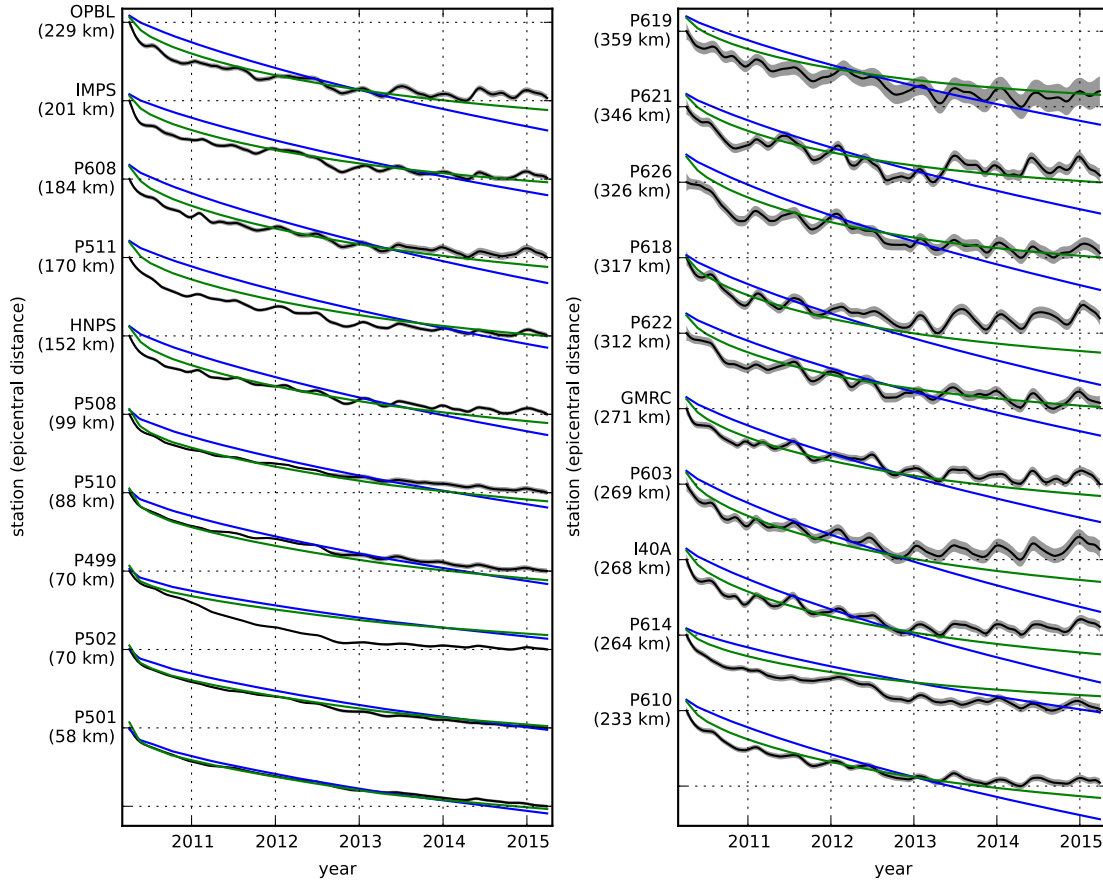
Rather than exploring a Burgers rheology mantle, which introduces two new parameters that need to be estimated, η_K and μ_K , we first consider a Zener rheology for the mantle, which only introduces one additional unknown parameter, μ_K . We assume that the lower crust still has a Maxwell rheology. The steady-state viscosity, η_M , in the crust and the transient viscosity, η_K , in the mantle are set equal to the inferred effective viscosities. We then estimate the ratio of shear moduli, $\frac{\mu_K}{\mu}$. We compute nine different sets of Green's functions, f and g , using Pylith, where we assume values of $\frac{\mu_K}{\mu}$ ranging from 0 to 1. The former being a degenerate case where the Zener model reduces to the above Maxwell model. We estimate coseismic slip and afterslip for each realization of $\frac{\mu_K}{\mu}$. The shear moduli ratio that yields to best prediction to the observed postseismic displacements is found to be 0.375 with a misfit of $\bar{\chi}^2 = 31.2$ (Figure 13). The improvement in the Zener model over the Maxwell model can be clearly seen in the fit to the far-field data (Figure 14). The Zener model does a significantly better job at explaining the transient rate of far-field deformation throughout the 5 years.

Because we are able to adequately describe the available 5 years of postseismic deformation with a Zener model, we do not find it necessary to explore the parameter space for a more complicated Burgers rheology. However, since the Zener model is a Burgers model with an infinite steady-state viscosity, we can conclude that any Burgers rheology that has a transient viscosity consistent with that found in Section 3.2 and a steady-state viscosity of $\gtrsim 10^{20}$ Pa s, which is effectively infinite on the time scale of 5 years, would also be able to satisfactorily describe the observable postseismic deformation.

The regularized inference of coseismic slip and afterslip for our preferred Zener model is shown in Figure 15, and the predicted postseismic displacements are shown Figures 4, 5 and 14. Overall, the trends in the near-field and far-field transient deformation are accurately described by our preferred model. In particular, the trends in far-field deformation are much better described by our preferred Zener model than either an elastic model or a model with a Maxwell viscoelastic mantle (Figure 14). There are a few areas where we have notable misfit. Most of our misfit is for the near-field stations in the Imperial Valley, and we attribute this misfit to our relatively simple fault geometry, which does not account for potential fault slip in the Imperial Valley triggered by the El Mayor-Cucapah earthquake [*Wei et al.*, 2011a, 2015]. In particular, we are unable to model the sustained, rapid rate of deformation at station P496, which



413 **Figure 13.** Mean chi-squared value for the best fitting slip model as a function of the transient shear modu-
 414 lus relative to the elastic shear modulus in a Zenner upper mantle. Large dot indicates our preferred ratio.



415 **Figure 14.** Observed postseismic displacements (black) and predicted postseismic displacements for the
 416 best fitting slip models when using a Maxwell (blue) and Zener (green) rheology in the upper mantle. The
 417 effective viscosities are the same for both models and are shown in Figure 11.

suggests that this station could be influenced by a more localized deformation mechanism than is considered in this study. Additionally, we see systematic misfit in the later postseismic period west of the Landers and Hector Mine earthquakes, which may be the result of unmodelled postseismic deformation resulting from those earthquakes. Lastly, there are clear discrepancies between the observed and predicted vertical deformation following the first year after the El Mayor Cucapah earthquake. We observe a broad uplift throughout Southern California, which is inconsistent with any postseismic model.

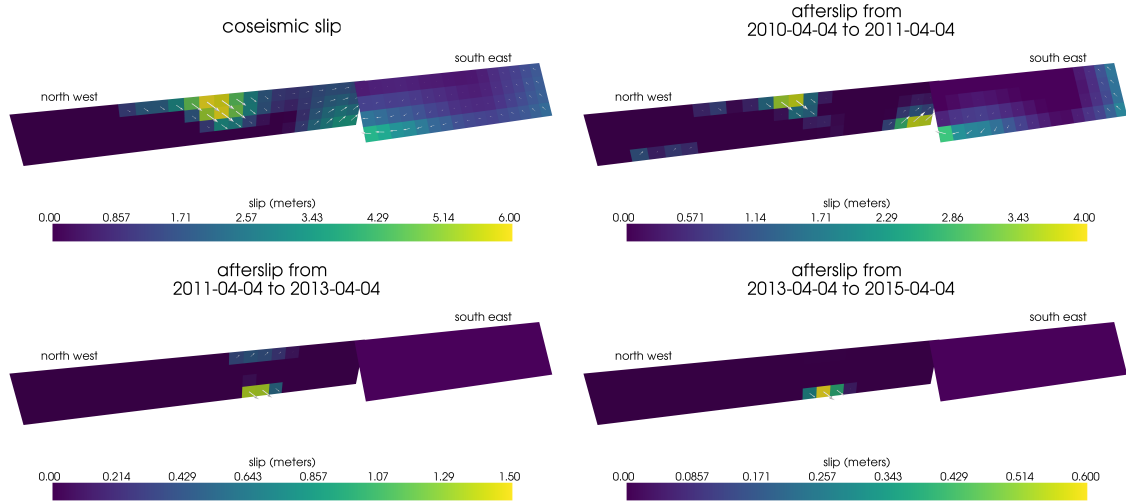


Figure 15. Inferred coseismic slip and afterslip when assuming a Maxwell rheology in the lower crust and a Zener rheology in the upper mantle. η_K in the mantle and η_M in the crust are set equal to the effective viscosities from Figure 11. We use $\frac{\mu_K}{\mu} = 0.375$ in the upper mantle.

The inferred coseismic potency is $3.0 \times 10^9 \text{ m}^3$, equivalent to a Mw7.26 earthquake, and the potency of 5 years of afterslip is $1.1 \times 10^9 \text{ m}^3$. Most of the afterslip in our preferred model occurs within the first year after the earthquake with a significant amount inferred to be shallow and in the Sierra Cucapah. The afterslip within the first year is accounting for the most rapid near-field transient deformation. After 1 year, afterslip is inferred to be deeper down on the Sierra Cucapah segment, which is describing much of the sustained near-field postseismic deformation. We emphasize, that the GPS station closest to our inferred afterslip, P496, is still about 30 km away, which is too far away for us to conclusively argue for sustained localized deformation rather shallow distributed deformation. The deep afterslip inferred after 1 year could potentially be describing deformation resulting from lower crustal flow. To test this, we have modified our preferred model by decreasing the lower crustal viscosity from $5.91 \times 10^{19} \text{ Pa s}$ to $1 \times 10^{19} \text{ Pa s}$, which is still consistent with our viscosity inference from Section 3.2, and inverted for fault slip. We find that a model with a weaker lower crust adequately describes the postseismic displacements without any afterslip after 1 year, while still requiring about the same amount of afterslip over the first year. We do believe that the early shallow afterslip on the Sierra Cucapah segment is a robust feature in our preferred model, while we are not confident in our inference of later deep afterslip.

4 Discussion

It has long been recognized that deep afterslip and viscoelastic relaxation following an upper crustal earthquake can result in similar horizontal ground deformation at the surface [e.g. Savage, 1990; Pollitz *et al.*, 2001; Hearn, 2003; Feigl and Thatcher, 2006]. The similarity of the horizontal postseismic deformation results in a non-uniqueness in inferences of afterslip

467 or viscoelastic relaxation. In contrast, the spatial pattern of vertical postseismic deformation
 468 has been proposed to be a discriminant between deep afterslip and viscoelastic relaxation [e.g.
 469 *Pollitz et al.*, 2001; *Hearn*, 2003]. It is, however, important to note that patterns of vertical de-
 470 formation are very sensitive to the depth-dependence of viscosity below the upper crust [?*Het-*
 471 *land and Zhang*, 2014]. The similarity between deformation resulting from deep afterslip and
 472 viscoelastic relaxation of coseismic stresses is different from the ill-posedness described in Sec-
 473 tion 3.2. In our method, any inferred afterslip will also mechanically drive additional viscoelas-
 474 tic relaxation. The horizontal deformation resulting from deep afterslip will generally be in
 475 the opposite direction as horizontal deformation resulting from viscoelastic relaxation of sub-
 476 sequent stresses in the lower crust (Figure 9). As a result, there is a trade-off between infer-
 477 ences of deep afterslip and lower crustal viscosity. In our synthetic tests in ?, we have found
 478 that inverting surface deformation for afterslip and viscosity within the same depth interval
 479 tends to result in overestimated afterslip and an underestimated viscosity at that depth.

480 Most postseismic studies assume Maxwell viscoelasticity in the lower crust and upper
 481 mantle [e.g. *Nur and Mavko*, 1974; *Pollitz et al.*, 2000; *Hetland*, 2003; *Freed et al.*, 2006; *John-*
 482 *son et al.*, 2009; *Hearn et al.*, 2009], which is the simplest viscoelastic rheologic model. In South-
 483 ern California, postseismic studies following the Landers [*Pollitz et al.*, 2000], Hector Mine
 484 [*Pollitz et al.*, 2001], and El Mayor-Cucapah earthquake [*Spinler et al.*, 2015; *Rollins et al.*, 2015],
 485 have assumed Maxwell viscoelasticity in the lithosphere and asthenosphere and have inferred
 486 upper mantle viscosities on the order of 10^{17} to 10^{18} Pa s and lower crust viscosities $\gtrsim 10^{19}$
 487 Pa s. These postseismic studies are consistent with *Kaufmann and Amelung* [2000] and *Cava-*
 488 *alié et al.* [2007], who found that an upper mantle viscosity of 10^{18} Pa s and a crustal viscos-
 489 ity $\gtrsim 10^{20}$ Pa s are necessary to describe subsidence resulting from changes in loading from
 490 Lake Mead. This isostatic adjustment is a process with similar spatial and temporal scales as
 491 postseismic deformation, and thus the inferred viscosities of these two types of studies would
 492 likely agree. While these studies found viscosities that are consistent with our effective vis-
 493 cosities from Section 3.2, they are inconsistent with viscosity estimates made from geophys-
 494 ical processes that occur over longer time scales. For example, *Lundgren et al.* [2009] found
 495 that lower crust and upper mantle viscosities on the order of 10^{21} and 10^{19} Pa s, respectively,
 496 are needed to describe interseismic deformation along the Southern San Andreas fault zone
 497 in the Salton Sea region. An even higher mantle viscosity, on the order of 10^{20} Pa s, is re-
 498 quired to describe isostatic adjustment resulting from the draining of Lake Bonneville, which
 499 occurs on the time scales of 10^4 years [*Crittenden*, 1967; *Bills and May*, 1987].

500 An additional deficiency with the Maxwell rheology is that it predicts a steady decay
 501 in the rate of postseismic deformation over time, which fails to describe the commonly ob-
 502 served rapid early transience followed by a relatively steady rate of postseismic deformation.
 503 One could explain the early transient postseismic deformation with fault creep and the later
 504 phase with relaxation in a Maxwell viscoelastic lower crust and upper mantle [e.g *Hearn et al.*,
 505 2009; *Johnson et al.*, 2009]. However, postseismic deformation at distances greater than ~ 200
 506 km from the El Mayor-Cucapah epicentre can only be attributed to viscoelastic relaxation [*Freed*
 507 *et al.*, 2007] and we have demonstrated that the far-field deformation cannot be explained with
 508 a Maxwell rheology (Figure 14).

509 We found that a Zener rheology in the upper mantle with a transient viscosity of $\sim 10^{18}$
 510 Pa s does a noticeably better job at predicting far-field postseismic deformation. A general-
 511 ization of the Zener viscoelastic model, schematically represented as several Kelvin elements
 512 connected in series, is commonly used to describe seismic attenuation [*Liu et al.*, 1976]. The
 513 highest viscosity needed to describe seismic attenuation is on the order of 10^{16} Pa s [*Yuen and*
 514 *Peltier*, 1982] which has a characteristic relaxation time on the order of days. Even though
 515 our inferred transient viscosity is orders of magnitude larger than that required for seismic at-
 516 tenuation models, the two models are not incompatible. Rather, the delayed elasticity in seis-
 517 mic attenuation models occurs on such short time scales that it can be considered part of the
 518 instantaneous elastic phase of deformation associated with the preferred Zener model in this
 519 study.

520 Of course, it has long been recognized that a Zener rheology provides an incomplete de-
 521 scriptions of the asthenosphere, as it does not have the fluid-like behaviour required to explain
 522 isostatic rebound or convection in the mantle [O'Connell, 1971]. Yuen and Peltier [1982] pro-
 523 posed a Burgers rheology with a low transient viscosity ($\eta_K \approx 10^{16}$ Pa s) and high steady-
 524 state viscosity ($\eta_M \approx 10^{21}$ Pa s) to describe both seismic attenuation and long term geologic
 525 processes. The justification of a Burger's rheology mantle is further supported by laboratory
 526 experiments on olivine [Chopra, 1997]. Pollitz [2003] sought to describe postseismic defor-
 527 mation following Hector Mine with a Burgers rheology mantle and they found a best fitting
 528 transient viscosity of 1.6×10^{17} Pa s and steady-state viscosity of 4.6×10^{18} Pa s. While
 529 the Burgers rheology was introduced as a means of bridging the gap between relaxation ob-
 530 served in long and short term geophysical processes, the inferred steady state viscosity from
 531 Pollitz [2003] is still inconsistent with the Maxwell viscosities inferred from earthquake cy-
 532 cle and lake loading studies. The transient viscosity inferred by Pollitz [2003] is constrained
 533 by the earliest phase of postseismic deformation following the Hector Mine earthquake. While
 534 Pollitz [2003] ruled out deep afterslip as an alternative mechanism based on inconsistent ver-
 535 tical deformation, it is still possible to successfully describe all components of early postseis-
 536 mic deformation following the Hector Mine earthquake with afterslip at seismogenic depths
 537 [Jacobs et al., 2002]. It is then possible that the preferred rheologic model from Pollitz [2003]
 538 was biased towards inferring a particularly low transient viscosity by neglecting to account for
 539 afterslip. This is in contrast to the present study, where we have inferred a lithospheric vis-
 540 cosity structure simultaneously with afterslip. We also argue that a transient rheology is nec-
 541 essary to explain postseismic deformation; however, our preferred transient viscosity of $\sim 10^{18}$
 542 Pa s in the mantle is an order of magnitude larger than the transient viscosity found by Pol-
 543 litz [2003]. Since a Zener model is able to describe the available postseismic deformation fol-
 544 lowing the El Mayor-Cucapah earthquake, any Burgers rheology with a steady-state viscous-
 545 ity that is $\gtrsim 10^{20}$ Pa s, effectively infinite over 5 years, would also be able to describe the
 546 postseismic deformation. Such a Burgers model might then be consistent with the steady state
 547 viscosities necessary for lake loading, interseismic deformation, and mantle dynamics.

548 5 Conclusion

549 We have extracted a filtered and smoothed estimate of postseismic deformation follow-
 550 ing the El Mayor-Cucapah earthquake from GPS displacements time series. We have treated
 551 postseismic deformation as a stochastic process where we did not presume any characteris-
 552 tic shape of the postseismic time series. We can observe transient postseismic deformation at
 553 distances of ~ 400 km from the El Mayor-Cucapah epicenter which is largely undetectable af-
 554 ter about 3 years. Near-field deformation exhibits transience that decays to a sustained, ele-
 555 vated rate after about 1 to 2 year. We found that the near-field transient deformation can be
 556 explained with shallow afterslip and the sustained rate of near field deformation can either be
 557 explained with continued afterslip or relaxation in a lower crustal with a viscosity of $\sim 10^{19}$
 558 Pa s. Far-field transient deformation can be more definitively ascribed to viscoelastic relax-
 559 ation at depths greater than ~ 60 km. Beneath that depth, a transient viscosity of $\sim 10^{18}$ Pa s
 560 is required to describe the rate of far-field deformation throughout the 5 years considered in
 561 this study. By describing the available postseismic deformation with a transient rheology in
 562 the mantle, our preferred model does not conflict with the generally higher steady-state vis-
 563 cosities inferred from geophysical processes occurring over longer time scales.

564 Acknowledgements

565 We thank Andy Freed for an illuminating discussion on the data used in this study. This
 566 material is based on EarthScope Plate Boundary Observatory data services provided by UN-
 567 AVCO through the GAGE Facility with support from the National Science Foundation (NSF)
 568 and National Aeronautics and Space Administration (NASA) under NSF Cooperative Agree-
 569 ment No. EAR-1261833. This material is based upon work supported by the National Science
 570 Foundation under Grant Numbers EAR 1045372 and EAR 1245263.

571 **References**

- 572 Aagaard, B. T., M. G. Knepley, and C. A. Williams (2013), A domain decomposition
 573 approach to implementing fault slip in finite-element models of quasi-static and dy-
 574 namic crustal deformation, *Journal of Geophysical Research: Solid Earth*, 118, doi:
 575 10.1002/jgrb.50217.
- 576 Argus, D. F., M. B. Heflin, G. Peltzer, F. Crampé, and F. H. Webb (2005), Interseismic
 577 strain accumulation and anthropogenic motion in metropolitan Los Angeles, *Journal of*
 578 *Geophysical Research: Solid Earth*, 110(4), 1–26, doi:10.1029/2003JB002934.
- 579 Aster, R. C., B. Borchers, and C. H. Thurber (2011), Parameter Estimation and Inverse
 580 Problems, vol. 90, Academic Press.
- 581 Bawden, G. W., W. Thatcher, R. S. Stein, K. W. Hudnut, and G. Peltzer (2001), Tectonic
 582 contraction across Los Angeles after removal of groundwater pumping effects., *Nature*,
 583 412(August), 812–815, doi:10.1038/35090558.
- 584 Bills, B. G., and G. M. May (1987), Lake Bonneville: Constraints on Lithospheric Thick-
 585 ness and Upper Mantle Viscosity From Isostatic Warping of Bonneville, Provo, and
 586 Gilbert Stage Shorelines, *Journal of Geophysical Research-Solid Earth and Planets*,
 587 92(B11), 11,493–11,508, doi:10.1029/JB092iB11p11493.
- 588 Çakir, Z., S. Ergintav, H. Özener, U. Dogan, A. M. Akoglu, M. Meghraoui, and
 589 R. Reilinger (2012), Onset of aseismic creep on major strike-slip faults, *Geology*,
 590 40(12), 1115–1118, doi:10.1130/G33522.1.
- 591 Cavalié, O., M. P. Doin, C. Lasserre, and P. Briole (2007), Ground motion measurement in
 592 the Lake Mead area, Nevada, by differential synthetic aperture radar interferometry time
 593 series analysis: Probing the lithosphere rheological structure, *Journal of Geophysical*
 594 *Research: Solid Earth*, 112(3), 1–18, doi:10.1029/2006JB004344.
- 595 Cetin, E., Z. Çakir, M. Meghraoui, S. Ergintav, and A. M. Akoglu (2014), Extent and
 596 distribution of aseismic slip on the İsmetpasa segment of the North Anatolian Fault
 597 (Turkey) from Persistent Scatterer InSAR, *Geochemistry, Geophysics, Geosystems*, 15,
 598 doi:10.1002/2014GC005307.Received.
- 599 Chopra, P. N. (1997), High-temperature transient creep in olivine rocks, *Tectonophysics*,
 600 279, 93–111, doi:10.1016/S0040-1951(97)00134-0.
- 601 Crittenden, M. (1967), Viscosity and Finite Strength of the Mantle as Determined from
 602 Water and Ice Loads*, *Geophysical Journal of the Royal Astronomical ...*, pp. 261–279,
 603 doi:10.1111/j.1365-246X.1967.tb06243.x.
- 604 Davis, J. L., B. P. Wernicke, and M. E. Tamisiea (2012), On seasonal signals in geode-
 605 tic time series, *Journal of Geophysical Research: Solid Earth*, 117(1), 1–10, doi:
 606 10.1029/2011JB008690.
- 607 Feigl, K. L., and W. Thatcher (2006), Geodetic observations of post-seismic transients in
 608 the context of the earthquake deformation cycle, *Comptes Rendus - Geoscience*, 338,
 609 1012–1028, doi:10.1016/j.crte.2006.06.006.
- 610 Fletcher, J. M., O. J. Teran, T. K. Rockwell, M. E. Oskin, K. W. Hudnut, K. J. Mueller,
 611 R. M. Spelz, S. O. Akciz, E. Masana, G. Faneros, E. J. Fielding, S. Leprince, A. E.
 612 Morelan, J. Stock, D. K. Lynch, A. J. Elliott, P. Gold, J. Liu-Zeng, A. González-
 613 Ortega, A. Hinojosa-Corona, and J. González-García (2014), Assembly of a large
 614 earthquake from a complex fault system: Surface rupture kinematics of the 4 April
 615 2010 El Mayor-Cucapah (Mexico) Mw 7.2 earthquake, *Geosphere*, 10(4), 797–827,
 616 doi:10.1130/GES00933.1.
- 617 Freed, A. M., R. Bürgmann, E. Calais, J. Freymueller, and S. Hreinsdóttir (2006), Impli-
 618 cations of deformation following the 2002 Denali, Alaska, earthquake for postseismic
 619 relaxation processes and lithospheric rheology, *Journal of Geophysical Research: Solid*
 620 *Earth*, 111, 1–23, doi:10.1029/2005JB003894.
- 621 Freed, A. M., R. Bürgmann, and T. Herring (2007), Far-reaching transient motions after
 622 Mojave earthquakes require broad mantle flow beneath a strong crust, *Geophysical*
 623 *Research Letters*, 34, 1–5, doi:10.1029/2007GL030959.

- 624 Gonzalez-Ortega, A., Y. Fialko, D. Sandwell, F. A. Nava-pichardo, J. Fletcher,
 625 J. Gonzalez-garcia, B. Lipovsky, M. Floyd, and G. Funning (2014), El Mayor-
 626 Cucapah (Mw7.2) earthquake: early near-field postseismic deformation from In-
 627 Sar and GPS observations, *Journal of Geophysical Research*, **119**, 1482–1497, doi:
 628 10.1002/2013JB010193.Received.
- 629 Hauksson, E., J. Stock, K. Hutton, W. Yang, J. A. Vidal-Villegas, and H. Kanamori
 630 (2011), The 2010 Mw 7.2 El mayor-cucapah earthquake sequence, Baja Califor-
 631 nia, Mexico and Southernmost California, USA: Active seismotectonics along the
 632 Mexican pacific margin, *Pure and Applied Geophysics*, **168**(3918), 1255–1277, doi:
 633 10.1007/s00024-010-0209-7.
- 634 Hearn, E. H. (2003), What can GPS data tell us about the dynamics of post-seismic defor-
 635 mation ?, (2003), 753–777.
- 636 Hearn, E. H., S. McClusky, S. Ergintav, and R. E. Reilinger (2009), Izmit earthquake post-
 637 seismic deformation and dynamics of the North Anatolian Fault Zone, *Journal of Geo-
 638 physical Research: Solid Earth*, **114**(August 2008), 1–21, doi:10.1029/2008JB006026.
- 639 Hetland, E. A. (2003), Postseismic relaxation across the Central Nevada Seismic Belt,
 640 *Journal of Geophysical Research*, **108**(Figure 2), 1–13, doi:10.1029/2002JB002257.
- 641 Hetland, E. A., and G. Zhang (2014), Effect of shear zones on post-seismic deformation
 642 with application to the 1997 Mw 7.6 manyi earthquake, *Geophysical Journal Interna-
 643 tional*, **198**, 259–269, doi:10.1093/gji/ggu127.
- 644 Hines, T. T., and E. A. Hetland (2013), Bias in estimates of lithosphere viscosity from
 645 interseismic deformation, *Geophysical Research Letters*, **40**(16), 4260–4265, doi:
 646 10.1002/grl.50839.
- 647 Hines, T. T., and E. A. Hetland (2016), Rapid and simultaneous estimation of fault slip
 648 and heterogeneous lithospheric viscosity from post-seismic deformation, *Geophysical
 649 Journal International*, **204**(1), 569–582, doi:10.1093/gji/ggv477.
- 650 Jacobs, A., D. Sandwell, Y. Fialko, and L. Sichoix (2002), The 1999 (Mw7.1) Hector
 651 Mine, California, Earthquake: Near-Field Postseismic Deformation from ERS Interfer-
 652 ometry, *Bulletin of the Seismological Society of America*, **92**(May), 1433–1442.
- 653 Johnson, K. M., and P. Segall (2004), Viscoelastic earthquake cycle models with deep
 654 stress-driven creep along the San Andreas fault system, *Journal of Geophysical Research
 655 B: Solid Earth*, **109**, 1–19, doi:10.1029/2004JB003096.
- 656 Johnson, K. M., R. Bürgmann, and J. T. Freymueller (2009), Coupled afterslip and vis-
 657 coelastic flow following the 2002 Denali Fault, Alaska earthquake, *Geophysical Journal
 658 International*, **176**(3), 670–682, doi:10.1111/j.1365-246X.2008.04029.x.
- 659 Jónsson, S., P. Segall, R. Pedersen, and G. Bjornsson (2003), Post-earthquake ground
 660 movements correlated to pore-pressure transients, *Nature*, **424**(July), 179–183, doi:
 661 10.1038/nature01758.1.
- 662 Kaufmann, G., and F. Amelung (2000), Reservoir-induced deformation and continental
 663 rheology in vicinity of Lake Mead, Nevada, *Journal of Geophysical Research*, **105**(B7),
 664 16,341, doi:10.1029/2000JB900079.
- 665 Kroll, K. A., E. S. Cochran, K. B. Richards-Dinger, and D. F. Sumy (2013), Aftershocks
 666 of the 2010 Mw 7.2 El Mayor-Cucapah earthquake reveal complex faulting in the Yuha
 667 Desert, California, *Journal of Geophysical Research: Solid Earth*, **118**(October), 6146–
 668 6164, doi:10.1002/2013JB010529.
- 669 Lekic, V., S. W. French, and K. M. Fischer (2011), Lithospheric Thinning Beneath Rifted
 670 Regions of Southern California, *Science*, **334**(November), 783–787.
- 671 Liu, H.-P., D. L. Anderson, and H. Kanamori (1976), Velocity dispersion due to anelastic-
 672 ity; implications for seismology and mantle composition, *Geophysical Journal Interna-
 673 tional*, **47**(1), 41–58, doi:10.1111/j.1365-246X.1976.tb01261.x.
- 674 Lundgren, P., E. A. Hetland, Z. Liu, and E. J. Fielding (2009), Southern San Andreas-San
 675 Jacinto fault system slip rates estimated from earthquake cycle models constrained by
 676 GPS and interferometric synthetic aperture radar observations, *Journal of Geophysical
 677 Research: Solid Earth*, **114**(2), 1–18, doi:10.1029/2008JB005996.

- 678 McGuire, J. J., and P. Segall (2003), Imaging of aseismic fault slip transients recorded
 679 by dense geodetic networks, *Geophysical Journal International*, 155(3), 778–788, doi:
 680 10.1111/j.1365-246X.2003.02022.x.
- 681 Meade, B. J., and B. H. Hager (2005), Block models of crustal motion in southern Cal-
 682 ifornia constrained by GPS measurements, *Journal of Geophysical Research B: Solid*
 683 *Earth*, 110, 1–19, doi:10.1029/2004JB003209.
- 684 Murray, J. R., and P. Segall (2005), Spatiotemporal evolution of a transient slip event on
 685 the San Andreas fault near Parkfield, California, *Journal of Geophysical Research : Solid*
 686 *Earth*, 110(9), 1–12, doi:10.1029/2005JB003651.
- 687 Nur, A., and G. Mavko (1974), Postseismic viscoelastic rebound, *Science*, 183(4121),
 688 204–206, doi:10.1038/098448b0.
- 689 O'Connell, R. J. (1971), Rheology of the Mantle, *EOS, Transactions, American Geophys-*
 690 *ical Union*, 52, 140–142.
- 691 Oskin, M. E., J. R. Arrowsmith, A. Hinojosa Corona, A. J. Elliott, J. M. Fletcher, E. J.
 692 Fielding, P. O. Gold, J. J. Gonzalez Garcia, K. W. Hudnut, J. Liu-Zeng, and O. J. Teran
 693 (2012), Near-field deformation from the El Mayor-Cucapah earthquake revealed by
 694 differential LIDAR, *Science*, 335(6069), 702–705, doi:10.1126/science.1213778.
- 695 Pollitz, F. C. Wicks, and W. Thatcher (2001), Mantle Flow Beneath a Continental Strike-
 696 Slip Fault : Postseismic Deformation After the 1999 Hector Mine Earthquake, *Science*,
 697 1814(2001), 1814–1818, doi:10.1126/science.1061361.
- 698 Pollitz, F. F. (2003), Transient rheology of the uppermost mantle beneath the Mo-
 699 jave Desert, California, *Earth and Planetary Science Letters*, 215, 89–104, doi:
 700 10.1016/S0012-821X(03)00432-1.
- 701 Pollitz, F. F., G. Peltzer, and R. Bürgmann (2000), Mobility of continental mantle: Evi-
 702 dence from postseismic geodetic observations following the 1992 Landers earthquake,
 703 *Journal of Geophysical Research*, 105(1999), 8035, doi:10.1029/1999JB900380.
- 704 Pollitz, F. F., R. Bürgmann, and W. Thatcher (2012), Illumination of rheological mantle
 705 heterogeneity by the M7.2 2010 El Mayor-Cucapah earthquake, *Geochemistry, Geo-*
 706 *physics, Geosystems*, 13(6), 1–17, doi:10.1029/2012GC004139.
- 707 Rauch, H. E., F. Tung, and C. T. Striebel (1965), Maximum likelihood estimates of linear
 708 dynamic systems, *AIAA Journal*, 3(8), 1445–1450.
- 709 Riva, R. E. M., and R. Govers (2009), Relating viscosities from postseismic relaxation to
 710 a realistic viscosity structure for the lithosphere, *Geophysical Journal International*, 176,
 711 614–624, doi:10.1111/j.1365-246X.2008.04004.x.
- 712 Rollins, C., S. Barbot, and J.-P. Avouac (2015), Postseismic Deformation Following the
 713 2010 M7.2 El Mayor-Cucapah Earthquake : Observations , Kinematic Inversions , and
 714 Dynamic Models, *Pure and Applied Geophysics*, doi:10.1007/s00024-014-1005-6.
- 715 Savage, J. C. (1990), Equivalent strike-slip earthquake cycles in half-space and
 716 lithosphere-asthenosphere earth models, *Journal of Geophysical Research*, 95, 4873,
 717 doi:10.1029/JB095iB04p04873.
- 718 Savage, J. C., and J. L. Svart (2009), Postseismic relaxation following the 1992 M 7.3
 719 Landers and 1999 M 7.1 Hector Mine earthquakes , southern California, *Journal of*
 720 *Geophysical Research*, 114(B01401), doi:10.1029/2008JB005938.
- 721 Savage, J. C., J. L. Svart, and S. B. Yu (2005), Postseismic relaxation and transient creep,
 722 *Journal of Geophysical Research: Solid Earth*, 110, 1–14, doi:10.1029/2005JB003687.
- 723 Segall, P., and M. Mathews (1997), Time dependent inversion of geodetic data, *Journal of*
 724 *Geophysical Research*, 102.
- 725 Spinler, J. C., R. A. Bennett, C. Walls, L. Shawn, and J. J. G. Garcia (2015), As-
 726 sessing long-term postseismic deformation following the M7.2 4 April 2010, El
 727 Mayor-Cucapah earthquake with implications for lithospheric rheology in the
 728 Salton Trough, *Journal of Geophysical Research: Solid Earth*, 120, 3664–3679, doi:
 729 10.1002/2014JB011613.Received.
- 730 Wei, M., D. Sandwell, Y. Fialko, and R. Bilham (2011a), Slip on faults in the Imperial
 731 Valley triggered by the 4 April 2010 Mw 7.2 El Mayor-Cucapah earthquake revealed by

- 732 InSAR, *Geophysical Research Letters*, 38(January), 1–6, doi:10.1029/2010GL045235.
- 733 Wei, M., Y. Liu, Y. Kaneko, J. J. McGuire, and R. Bilham (2015), Dynamic triggering of
734 creep events in the Salton Trough, Southern California by regional M5.4 earthquakes
735 constrained by geodetic observations and numerical simulations, *Earth and Planetary
736 Science Letters*, 427, 1–10, doi:10.1016/j.epsl.2015.06.044.
- 737 Wei, S., E. Fielding, S. Leprince, A. Sladen, J.-P. Avouac, D. Helmberger, E. Hauksson,
738 R. Chu, M. Simons, K. Hudnut, T. Herring, and R. Briggs (2011b), Superficial sim-
739 plicity of the 2010 El MayorCucapah earthquake of Baja California in Mexico, *Nature
740 Geoscience*, 4(9), 615–618, doi:10.1038/ngeo1213.
- 741 Yuen, D. A., and W. R. Peltier (1982), Normal modes of the viscoelastic earth, *Geo-
742 physical Journal of the Royal Astronomical Society*, 69, 495–526, doi:10.1111/j.1365-
743 246X.1982.tb04962.x.